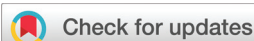


## RESEARCH ARTICLE

[View Article Online](#)  
[View Journal](#) | [View Issue](#)

 Cite this: *Inorg. Chem. Front.*, 2022, **9**, 5507

# Interface engineering of hierarchical P-doped NiSe/2H-MoSe<sub>2</sub> nanorod arrays for efficient hydrogen evolution†

 Xiaocheng Xu,<sup>a</sup> Rui Wang,<sup>a</sup> Sijie Chen,<sup>a</sup> Alex Trukhanov,<sup>b</sup> Yanxue Wu,<sup>c</sup> Lianyi Shao,<sup>b,\*a,d</sup> Le Huang<sup>\*a,d</sup> and Zhipeng Sun<sup>b,\*a</sup>

Developing non-noble metal-based electrocatalysts with excellent activity and stability for the hydrogen evolution reaction (HER) is crucial for the efficient electrolysis of water. Herein, self-supported three-dimensional (3D) P-doped NiSe/2H-MoSe<sub>2</sub> nanorod arrays (denoted as P-NiSe/MoSe<sub>2</sub>) were fabricated by a hydrothermal reaction and subsequent selenization and phosphorization processes. Benefiting from P doping, the synergistic effect of the heterostructures, and abundant active sites, the P-NiSe/MoSe<sub>2</sub> electrocatalyst exhibits excellent alkaline HER performance, with only 43 mV required to achieve 10 mA cm<sup>-2</sup> with a Tafel slope of 93.1 mV dec<sup>-1</sup>, even remaining stable at 10 mA cm<sup>-2</sup> for 30 hours. In addition, theoretical calculations show that the formation of the heterostructure and P doping optimize the H atom adsorption energies and accelerate electron transport, thus improving its performance in the HER. This work offers a hopeful route for the development of low-cost and efficient electrocatalysts through the simultaneous application of heterostructure engineering and heteroatom doping as well as a 3D structure.

 Received 12th July 2022,  
 Accepted 26th August 2022  
 DOI: 10.1039/d2qi01498j

[rsc.li/frontiers-inorganic](https://rsc.li/frontiers-inorganic)

## Introduction

The electrolysis of water has gained a lot of interest as a power conversion process for the efficient generation of H<sub>2</sub> from water or seawater to fulfil the energy demand and decrease carbon emissions due to the excessive usage of fossil fuels.<sup>1–3</sup> Unfortunately, the sluggish kinetics of water electrolysis requires the use of precious metal-based electrocatalysts such as Pt and Ru/IrO<sub>2</sub>. However, they cannot be applied in the industry on a large scale because of their low availability, high cost, and poor long-term stability.<sup>4–6</sup> Therefore, oxides,<sup>7</sup> carbides,<sup>8</sup> nitrides,<sup>9</sup> phosphides,<sup>10</sup> sulfides,<sup>11</sup> and selenides<sup>12</sup> containing transition metal elements have been extensively investigated as alternatives to noble metal electrocatalysts. Among them, transition metal selenides (TMSes) are prospective electrocatalysts because their special electronic structure facilitates electron transport and reaction occurrence.<sup>12,13</sup>

In recent years, various strategies have been used to prepare electrocatalysts with efficient electrocatalytic performance, such as heteroatom doping, interface engineering, phase engineering, defect engineering, and morphology control.<sup>14,15</sup> Heteroatom doping can improve the chemical environment of the active sites and the electronic state of the catalyst.<sup>16–18</sup> Zhu *et al.* prepared P-doped bimetallic NiSe<sub>2</sub>-MoSe<sub>2</sub> grown on carbon cloth, which exhibited outstanding HER activity due to P doping, which modulates the electronic structure and promotes charge accumulation and consumption.<sup>16</sup> In addition, the different components in a heterogeneous structure constructed by interface engineering can exhibit synergistic effects to enhance chemisorption and desorption at the interface.<sup>8,19,20</sup> A new heterostructure containing crystalline NiSe and amorphous MoSe<sub>x</sub> was developed by Feng *et al.* with increased electrical conductivity, improved multiphase balance, and enhanced stability through interface engineering.<sup>20</sup> However, the improvement of catalysts using only a single strategy is very limited, and therefore multiple strategies have been used to enhance the catalytic activity together. For example, Zhang *et al.* used interface engineering and heteroatom doping to prepare the Mo-NiS/Ni(OH)<sub>2</sub> bifunctional electrocatalyst with a heterogeneous structure,<sup>21</sup> Li *et al.* prepared the Au@MoS<sub>2</sub> heterogeneous structure with a unique wing shape *via* morphology modulation and interface engineering,<sup>22</sup> and Ma *et al.* used metal atom doping and phase engineering to prepare Mo<sub>2</sub>C catalysts with Co doping and Mo defects at the same time, which exhibited excellent HER performance.<sup>23</sup>

<sup>a</sup>School of Materials and Energy, Guangdong University of Technology, Guangzhou, 510006 Guangdong, China. E-mail: zpsunxj@gdut.edu.cn

<sup>b</sup>Functional Materials Centre, SSPA Scientific and Practical Materials Research Centre of NAS of Belarus, 19 P. Brovki St, 220072 Minsk, Belarus

<sup>c</sup>Analysis and Test Center, Guangdong University of Technology, Guangzhou, 510006 Guangdong, China

<sup>d</sup>Institute of Applied Physics and Materials Engineering, University of Macau, Macao SAR, 999078, China

† Electronic supplementary information (ESI) available. See DOI: <https://doi.org/10.1039/d2qi01498j>

Inspired by the above-mentioned research, we combined heteroatom doping and interface engineering to design the P-doped NiSe/2H-MoSe<sub>2</sub> electrocatalyst on NF with the structure of nanoparticles on nanorods. The obtained P-NiSe/MoSe<sub>2</sub> presents three advantages that favor electrocatalytic reactions. First, the three-dimensional (3D) hierarchical structure on nickel foam improves electrical conductivity, promotes the breakdown of small bubbles, and provides more active sites. Secondly, P doping modulates the electronic structures of both NiSe and 2H-MoSe<sub>2</sub>, which improves the electronic conductivity of the electrocatalyst. Finally, the heterostructure containing NiSe and 2H-MoSe<sub>2</sub> can promote the synergetic effect among the components and optimize the interfacial charge transport. Benefiting from P doping and heterostructure construction, P-NiSe/MoSe<sub>2</sub> exhibits excellent HER performance, with overpotentials of 43 mV and 182 mV at 10 mA cm<sup>-2</sup> and 100 mA cm<sup>-2</sup>, respectively, under alkaline conditions, exceeding the performance of most previously reported TMSes. This comprehensive strategy could encourage the development of new catalysts for the efficient hydrogen evolution reaction.

## Results and discussion

### Characterization of the electrocatalysts

P-NiSe/MoSe<sub>2</sub>@NF was synthesized in two steps (Fig. 1a), starting with the hydrothermal reaction of nickel foam, followed by selenization and P doping. Digital images of the pre-

pared samples are shown in Fig. S1,† demonstrating the color change in the P-NiSe/MoSe<sub>2</sub>@NF electrocatalyst from silver-white NF to green NiMoO<sub>4</sub>@NF to black P-NiSe/MoSe<sub>2</sub>@NF. SEM was used to investigate the microstructure and geometric morphologies of the as-synthesized materials. As shown in Fig. 1b and S2,† after hydrothermal treatment, the original smooth surface of NF was decorated with densely and uniformly distributed NiMoO<sub>4</sub> nanorods grown *in situ*. After selenization and P doping, the P-NiSe/MoSe<sub>2</sub>@NF catalyst still maintains the uniformly distributed nanorods in its structure (Fig. 1c and d), and it is worth noting that many nanoparticles appear on the nanorods compared to the smooth nanorods of the NiMoO<sub>4</sub> precursor. Fig. S3† shows the SEM images and EDS results of samples with different phosphorus doping amounts, while Table S1† presents the phosphorus doping amounts in the different samples. Compared with the uneven morphological structure of Ni<sub>x</sub>Se<sub>y</sub>@NF (Fig. S4†), the unique structure of nanorod arrays with nanoparticles has a larger specific surface area, thus allowing more active sites to be involved in the reaction. In addition, the wettability of P-NiSe/MoSe<sub>2</sub>@NF was examined by contact angle measurement. The drop stood stably over the face of NF, as seen in Fig. S5a,† but the drop rapidly penetrates P-NiSe/MoSe<sub>2</sub>@NF (Fig. S5b†), which indicates its superhydrophilicity. This superior structure of P-NiSe/MoSe<sub>2</sub>@NF not only brings the active surface sites in full contact with the electrolyte but also accelerates the detachment of bubbles, which facilitates the catalytic reaction.

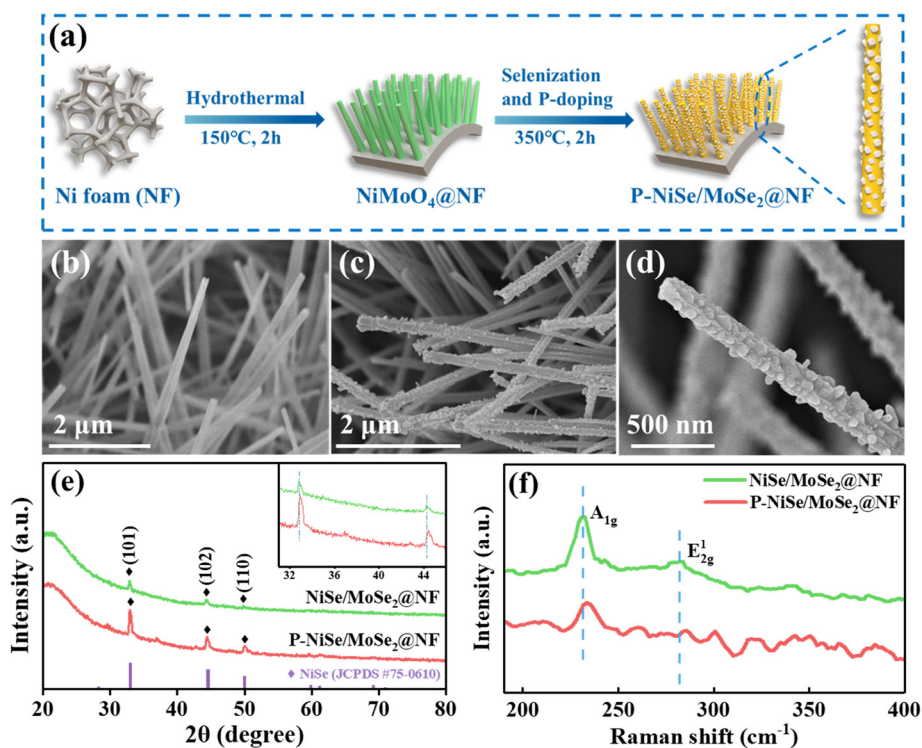


**Fig. 1** (a) Schematic of the synthesis of the P-NiSe/MoSe<sub>2</sub>@NF electrode. SEM images of (b) NiMoO<sub>4</sub>@NF and (c and d) P-NiSe/MoSe<sub>2</sub>@NF. (e) XRD patterns and (f) Raman spectra of NiSe/MoSe<sub>2</sub>@NF and P-NiSe/MoSe<sub>2</sub>@NF.

The phases of the samples were investigated by X-ray diffraction (XRD). The diffraction peaks of the as-prepared precursors match well with the standard XRD patterns of  $\text{NiMoO}_4 \cdot x\text{H}_2\text{O}$  and  $\text{Ni}(\text{OH})_2$  (Fig. S6<sup>†</sup>). As shown in Fig. 1e, the three peaks at  $32.8^\circ$ ,  $44.3^\circ$ , and  $49.7^\circ$  in the diffraction pattern of  $\text{NiSe}/\text{MoSe}_2@\text{NF}$  correspond to the (101), (102), and (110) planes of NiSe (JCPDS 75-0610). Similarly, the apparent peaks in  $\text{P-NiSe}/\text{MoSe}_2@\text{NF}$  can be indexed to NiSe (JCPDS 75-0610). Notably, the diffraction peaks of  $\text{P-NiSe}/\text{MoSe}_2@\text{NF}$  shift to a higher angle, indicating that P doping decreases the lattice parameters of  $\text{P-NiSe}/\text{MoSe}_2@\text{NF}$ .<sup>18,24</sup> The lack of diffraction peaks related to the molybdenum phase is due to the poor crystallinity of  $\text{MoSe}_2$ , which can be explained by Raman spectroscopy.<sup>25</sup> According to the Raman data (Fig. 1f),  $\text{NiSe}/\text{MoSe}_2@\text{NF}$  and  $\text{P-NiSe}/\text{MoSe}_2$  show characteristic peaks at 231 and 282  $\text{cm}^{-1}$ , respectively belonging to the vibration of  $A_{1g}$  and  $E_{2g}^1$  of  $2\text{H-MoSe}_2$ .<sup>26,27</sup> Therefore, we can reasonably conjecture that  $\text{NiSe}/\text{MoSe}_2@\text{NF}$  and  $\text{P-NiSe}/\text{MoSe}_2@\text{NF}$  contain the NiSe and  $2\text{H-MoSe}_2$  phases, which was confirmed by the subsequent TEM characterization. In comparison, the pattern of  $\text{Ni}_x\text{Se}_y@\text{NF}$  has several peaks that can be well-indexed to NiSe (JCPDS 75-0610),  $\text{Ni}_3\text{Se}_2$  (JCPDS 85-0754), and Ni (JCPDS 04-0850) (Fig. S7<sup>†</sup>). To observe the morphological details of the  $\text{P-NiSe}/\text{MoSe}_2@\text{NF}$  heterostructure, transmission electron microscopy (TEM) was used. It is observed that the  $\text{P-NiSe}/\text{MoSe}_2@\text{NF}$  catalyst is composed of nanorods with a diameter of about 131 nm that have many nanoparticles on their surface (Fig. 2a and b). As shown in Fig. 2c and d, it is observed that the (002) plane of  $2\text{H-MoSe}_2$  (JCPDS 29-0914) has lattice fringes of 0.643 nm and 0.646 nm, and the lattice

fringes of 0.260 nm and 0.165 nm belong to the (102) and (110) planes of  $2\text{H-MoSe}_2$  (JCPDS 29-0914), while the lattice fringes of 0.201 nm and 0.185 nm belong to the (102) and (110) planes of NiSe (JCPDS 75-0610). The selected area electron diffraction (SAED) image of  $\text{P-NiSe}/\text{MoSe}_2@\text{NF}$  shows the indexes for NiSe (100), NiSe (102), and  $2\text{H-MoSe}_2$  (103) (Fig. 2e). Moreover, energy dispersive spectroscopy (EDS) mapping shows the uniform distribution of the elements Ni, Mo, Se, and P (Fig. 2f–j). According to the XRD, Raman, and TEM results, the heterostructure of  $\text{NiSe}/2\text{H-MoSe}_2$  has been formed successfully, which may provide more active sites and further improve the HER performance.<sup>19,21</sup>

X-ray photoelectron spectroscopy (XPS) was used to further investigate the elemental composition and atomic valence of the materials. The doping of different elements changes the coordination environment of the host elements, leading to a change in binding energy.<sup>28</sup> Therefore, we hope to obtain information on the electronic structural evolution of the material after P doping from the XPS data. As shown in Fig. 3a, the peaks at 855.8 and 873.7 eV in the Ni 2p region of  $\text{NiSe}/\text{MoSe}_2@\text{NF}$  could be indexed to the Ni 2p<sub>3/2</sub> and Ni 2p<sub>1/2</sub> of Ni<sup>2+</sup> in NiSe,<sup>29,30</sup> while the other two peaks at 861.4 and 879.5 eV were attributed to satellite peaks.<sup>31,32</sup> In addition, the binding energy peaks at 853.2 and 870.5 eV belong to metallic Ni,<sup>33</sup> which is generally ascribed to the exposed nickel foam. It is worth noting that the binding energies of Ni<sup>2+</sup> 2p exhibit a positive shift of about 0.3 eV after P substitution, indicating that P doping modulates the electronic structure of  $\text{P-NiSe}/\text{MoSe}_2@\text{NF}$ , causing the electron density around the nickel atom to decrease.<sup>34,35</sup> In the Mo 3d spectra in Fig. 3b, the peaks at 229 and 232.2 eV correspond to

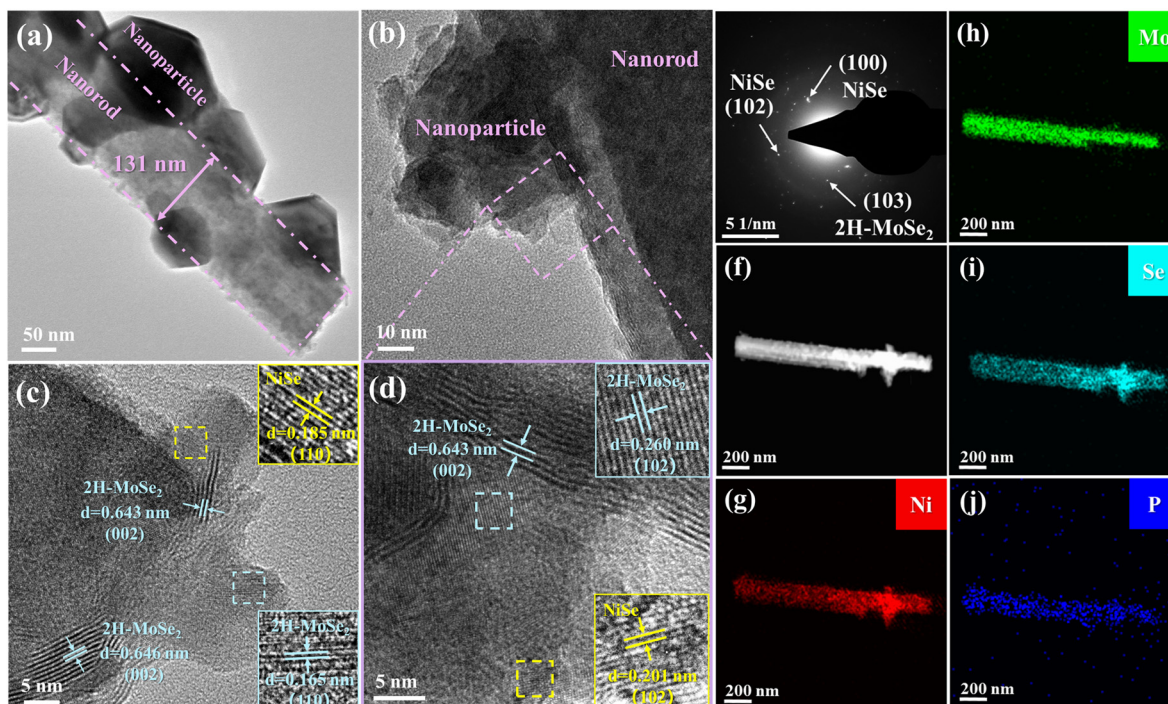


Fig. 2 (a and b) TEM images, (c and d) HRTEM images, (e) SAED image, and (f–j) elemental mapping of  $\text{P-NiSe}/\text{MoSe}_2@\text{NF}$ .

the Mo 3d<sub>5/2</sub> and Mo 3d<sub>3/2</sub> of Mo<sup>4+</sup>, respectively, confirming the presence of 2H-MoSe<sub>2</sub>.<sup>36</sup> Meanwhile, the peaks at 232.8 and 235.8 eV represent the appearance of Mo<sup>6+</sup>, which is due to partial oxidization in the air.<sup>37</sup> The other peak located at 229.9 eV is ascribed to the Se 3s of MoSe<sub>2</sub>.<sup>38</sup> It is found that in P-NiSe/MoSe<sub>2</sub>@NF, the binding energies of Mo<sup>4+</sup> 3d exhibit a negative shift by ~0.2 eV, indicating that P doping reduces the electron density on Mo.<sup>39,40</sup> In the case of the Se 3d spectrum (Fig. 3c), the two peaks of Se 3d<sub>5/2</sub> (54.5 eV) and Se 3d<sub>3/2</sub> (55.3 eV) reveal the presence of Se<sup>2-</sup> in NiSe and 2H-MoSe<sub>2</sub>,<sup>29,41</sup> while the peak located at 59 eV indicates the surface oxidation state of selenium.<sup>38</sup> For P-NiSe/MoSe<sub>2</sub>@NF, the two peaks of Se 3d show a negative shift of about 0.2 eV, suggesting an increase in electron occupation around the Se atom, resulting in an enhanced ability to provide electrons.<sup>42</sup> Furthermore, the peak at 133.7 eV in the P 2p spectrum (Fig. 3d) indicates the existence of P=O bonding, which may be caused by the inevitable contact of the sample with air.<sup>43,44</sup>

These results suggest that P doping can modulate the electronic structure and ionization state of the material, changing the electron density around Ni, Mo, and Se. These changes may optimize proton adsorption and increase the actual acceptor sites during the HER process, thus accelerating the catalytic reaction.<sup>45,46</sup>

### Electrocatalytic performance

In order to investigate the optimal amount of phosphorus doping, LSV tests were performed on the samples with different phosphorus doping amounts, and the results in Fig. S8† show that the best HER performance was achieved when the amount of sodium hypophosphite used was 20 mg.

The HER electrocatalytic performance of pure NF, NiMoO<sub>4</sub>@NF, Ni<sub>x</sub>Se<sub>y</sub>@NF, NiSe/MoSe<sub>2</sub>@NF, and P-NiSe/MoSe<sub>2</sub>@NF was evaluated. From the LSV curves (Fig. 4a), it is evident that Ni<sub>x</sub>Se<sub>y</sub>@NF, NiSe/MoSe<sub>2</sub>@NF, and P-NiSe/MoSe<sub>2</sub>@NF show better HER catalytic activity than the precursors NiMoO<sub>4</sub>@NF and pure NF. Obviously, P-NiSe/MoSe<sub>2</sub>@NF exhibits excellent HER electrocatalytic performance. P-NiSe/MoSe<sub>2</sub>@NF requires only 43 mV to reach 10 mA cm<sup>-2</sup>, a better result than those of Ni<sub>x</sub>Se<sub>y</sub>@NF (135 mV) and NiSe/MoSe<sub>2</sub>@NF (94 mV). This demonstrates the effective enhancement in HER performance *via* the combined effect of heteroatom doping and interface engineering. As seen in the quantitative bar chart (Fig. 4b), P-NiSe/MoSe<sub>2</sub>@NF needs only 182 mV to reach 100 mA cm<sup>-2</sup>, which is much better than most previously reported TMSes, as compared in Fig. 4c and Table S1.† The same result is obtained for the Tafel slopes (Fig. 4d), in which P-NiSe/MoSe<sub>2</sub>@NF exhibits a Tafel slope of 93.1 mV dec<sup>-1</sup>, smaller than those of pure NF (180.2 mV dec<sup>-1</sup>), NiMoO<sub>4</sub>@NF (161.9 mV dec<sup>-1</sup>), Ni<sub>x</sub>Se<sub>y</sub>@NF (145.3 mV dec<sup>-1</sup>), and NiSe/MoSe<sub>2</sub>@NF (114.4 mV dec<sup>-1</sup>), suggesting that the course of the HER in P-NiSe/MoSe<sub>2</sub>@NF is the Volmer–Heyrovsky mechanism.<sup>47</sup> The values of the exchange current density (*j*<sub>0</sub>) are obtained from the Tafel slopes (Fig. S9†). The *j*<sub>0</sub> value of P-NiSe/MoSe<sub>2</sub>@NF (3.549 mA cm<sup>-2</sup>) is higher than those of NiSe/MoSe<sub>2</sub>@NF (1.541 mA cm<sup>-2</sup>) and Ni<sub>x</sub>Se<sub>y</sub>@NF (1.195 mA cm<sup>-2</sup>). The Nyquist plots and the fitted results of all electrocatalysts (Fig. 5e and f) provide the solution resistance and charge transfer resistance of the electrocatalysts. The charge transfer resistance (*R*<sub>ct</sub>) value of P-NiSe/MoSe<sub>2</sub>@NF (3.11 Ω) is lower than those of pure NF (28.38 Ω), NiMoO<sub>4</sub>@NF (23.15 Ω), Ni<sub>x</sub>Se<sub>y</sub>@NF (10.71 Ω), and NiSe/MoSe<sub>2</sub>@NF (3.76 Ω), resulting

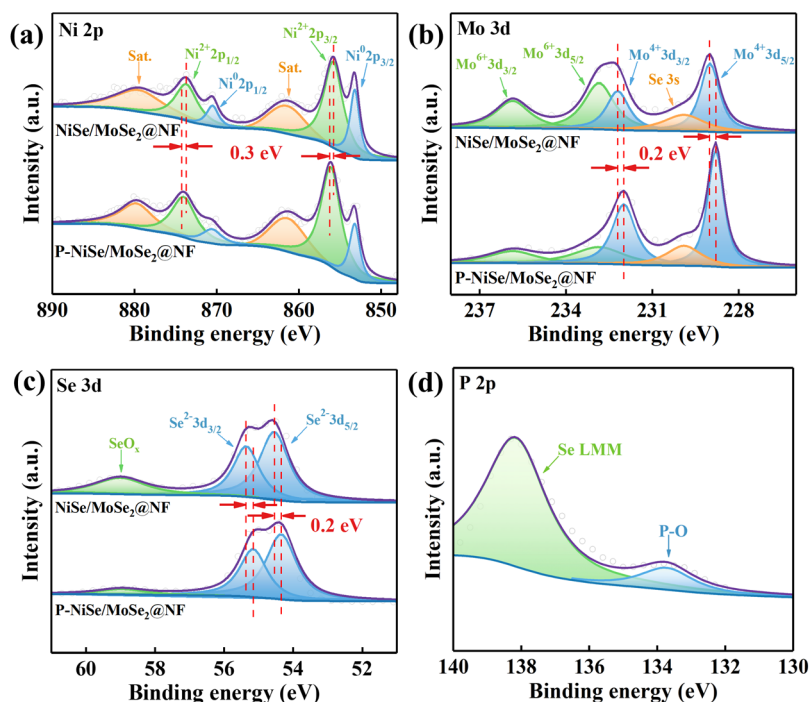
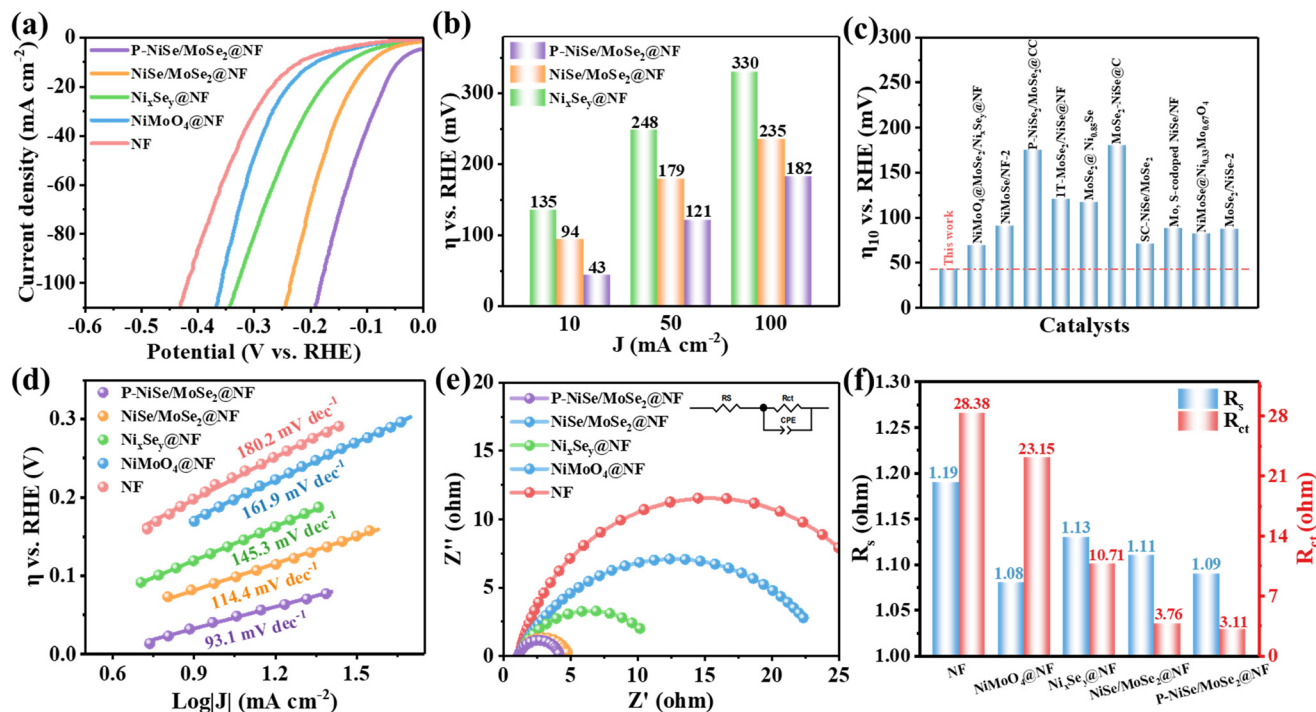


Fig. 3 XPS spectra of (a) Ni 2p, (b) Mo 3d, (c) Se 3d in NiSe/MoSe<sub>2</sub>@NF and P-NiSe/MoSe<sub>2</sub>@NF. (d) XPS spectrum of P 2p in P-NiSe/MoSe<sub>2</sub>@NF.



**Fig. 4** (a) LSV tests at a scan rate of 2 mV s<sup>-1</sup>. (b) Comparison of overpotentials at different current densities. (c) Comparison of the overpotentials of P-NiSe/MoSe<sub>2</sub>@NF and other selenide catalysts at a current density of 10 mA cm<sup>-2</sup>. (d) Tafel slopes. (e) Nyquist plots. (f) Fitted solution resistance and charge-transfer resistance of the catalysts.

in a faster charge transfer on the catalyst/electrolyte interface during the HER.

To further investigate the origin of the catalyst's performance, a series of CV tests were conducted under different scan rates (Fig. S10<sup>†</sup>). As shown in Fig. 5a, the area of the CV curve of P-NiSe/MoSe<sub>2</sub>@NF at a scan rate of 60 mV s<sup>-1</sup> is obviously larger than those of the other catalysts. Meanwhile, as seen in Fig. 5b, the calculated fit was obtained, and the  $C_{di}$  of P-NiSe/MoSe<sub>2</sub>@NF (133.69 mF cm<sup>-2</sup>) is higher than those of pure NF (1.94 mF cm<sup>-2</sup>), NiMoO<sub>4</sub>@NF (2.85 mF cm<sup>-2</sup>), Ni<sub>x</sub>Se<sub>y</sub>@NF (17.49 mF cm<sup>-2</sup>), and NiSe/MoSe<sub>2</sub>@NF (110.20 mF cm<sup>-2</sup>), suggesting that the heterostructure exposes more active sites, which is favorable to improving the HER catalytic activity. We further investigated the stability of P-NiSe/MoSe<sub>2</sub>@NF by chronopotentiometry (CP) measurements (Fig. 5c), which exhibits excellent stability for 30 hours under alkaline conditions at 10 mA cm<sup>-2</sup>, while the LSV curve showed only a small change. In addition, after 2000 CV cycles, the overpotential shifted by only 12 mV at 100 mA cm<sup>-2</sup> (Fig. 5d), again proving the excellent stability of P-NiSe/MoSe<sub>2</sub>@NF. SEM and XRD tests indicate that the material maintains its original structure and morphology after the stability test, which proves that it has a stable chemical composition and long-lasting catalytic properties (Fig. 5e and f).

### Catalytic mechanism

First-principles density functional theory (DFT) calculations were performed to elucidate the effect of the heterostructure

and P doping. The effect of interfacial coupling on the electronic structure of the NiSe/MoSe<sub>2</sub> heterostructure was first investigated, and the charge density is shown in Fig. 6a. The purple and yellow areas represent electron accumulation and electron depletion, respectively, from which charge transfer is observed at the interface between NiSe and 2H-MoSe<sub>2</sub>. The optimized geometric models with the possible adsorption sites for H\* of MoSe<sub>2</sub>, NiSe, NiSe/MoSe<sub>2</sub>, and P-NiSe/MoSe<sub>2</sub> are shown in Fig. S11<sup>†</sup>. Numerous studies have shown that the Gibbs free-energy of hydrogen adsorption ( $\Delta G_{H^*}$ ) on the surface of the catalyst can be used to evaluate the intrinsic activity of the catalyst towards the HER.<sup>23,48</sup> The nearer the value of  $|\Delta G_{H^*}|$  to zero, the easier the adsorption of H\*, which favors the HER process.<sup>40,49</sup> As shown in Table S3<sup>†</sup>, the lower  $\Delta G_{H^*}$  value of NiSe/MoSe<sub>2</sub> (Se site of NiSe, 0.17 eV) compared to those of MoSe<sub>2</sub> (Se site, 2.10 eV) and NiSe (Ni site, 0.23 eV; Se site, 0.22 eV) suggests that the formation of the heterostructure can reduce the hydrogen adsorption energy of the material. In Fig. 6b, the  $\Delta G_{H^*}$  value of P-NiSe/MoSe<sub>2</sub> (P site, 0.16 eV) is lower than that of NiSe/MoSe<sub>2</sub>, which indicates that P doping further optimizes the adsorption of hydrogen and thus improves the electrocatalytic activity. Meanwhile, the P atom is involved in the reaction as the main active site. In addition, we calculated the projected density of states (PDOS), as shown in Fig. S12<sup>†</sup>. The DOS around the Fermi level is critical to determining the HER electrochemical activity. The higher the density of states near the Fermi level, the more effective the charge transfer between the electrocatalyst and

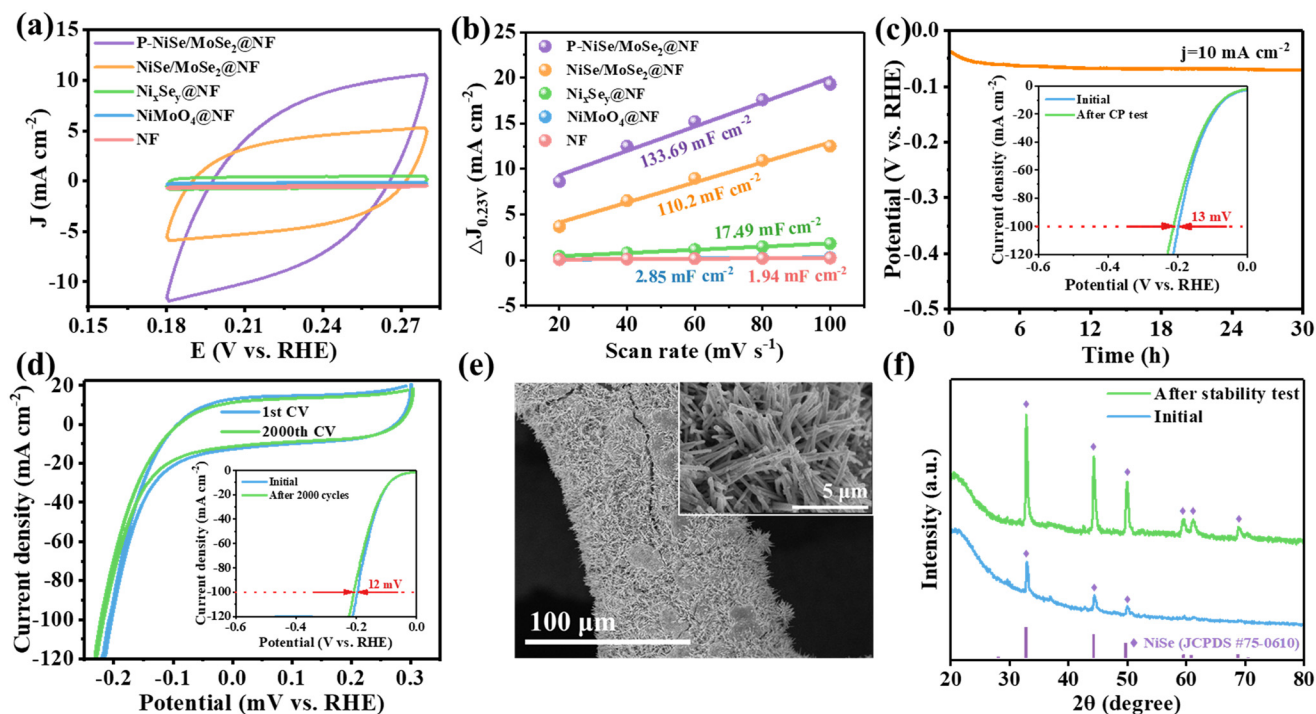


**Fig. 5** (a) CV curves of the catalysts at a scan rate of  $60 \text{ mV s}^{-1}$  (b) The approximate  $C_{dl}$  obtained by calculating the current density change at 0.23 V with different scan rates. (c) Chronopotentiometric curve of P-NiSe/MoSe<sub>2</sub>@NF for 30 h at  $10 \text{ mA cm}^{-2}$  (inset: polarization curves after the CP test). (d) The first CV cycle curve and 2000<sup>th</sup> CV cycle curve of the P-NiSe/MoSe<sub>2</sub>@NF catalyst (inset: polarization curves after CV for 2000 cycles). (e) SEM images and (f) XRD patterns of the P-NiSe/MoSe<sub>2</sub>@NF catalyst after the stability test.

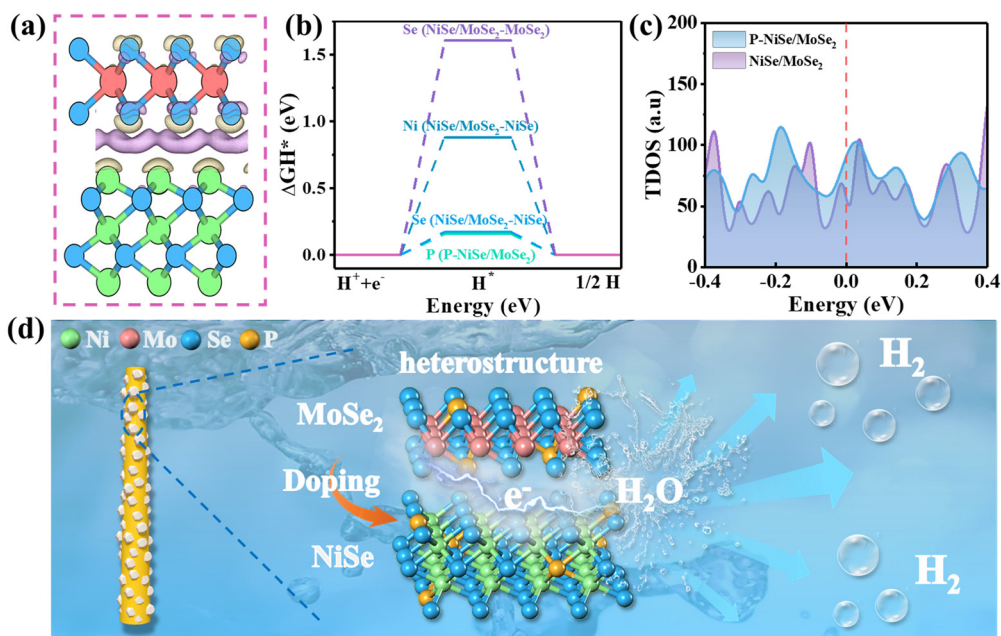


**Fig. 6** (a) Charge density difference at the interface of the NiSe/MoSe<sub>2</sub> heterostructure. (b) Gibbs free-energy diagrams of NiSe/MoSe<sub>2</sub> and P-NiSe/MoSe<sub>2</sub> for H adsorption ( $\text{H}^*$ ). (c) The calculated total electronic density of states (TDOS) of NiSe/MoSe<sub>2</sub> and P-NiSe/MoSe<sub>2</sub>. The Fermi level is set at 0 eV as a reference. (d) Hydrogen production from the P-NiSe/MoSe<sub>2</sub>@NF catalyst promoted by the comprehensive strategy of preparing a heterostructure and P doping.

adsorbed H atom.<sup>50,51</sup> As observed in Fig. 6c, the total density of states of P-NiSe/MoSe<sub>2</sub> is significantly higher than that of NiSe/MoSe<sub>2</sub>, which indicates that P doping accelerates electron transport and thus favors the charge transfer capability of the electrocatalyst in the HER process.

The HER performance of the material can be improved by using a combined strategy of interface engineering and heteroatom doping, as shown in Fig. 6e. The special morphology of nanoparticles on nanorods can increase the specific surface area, expose more active sites and promote bubble dissociation. *In situ* selenization on the precursor NiMoO<sub>4</sub> generates the NiSe and 2H-MoSe<sub>2</sub> heterostructure with rich interfaces, while P doping optimizes the hydrogen adsorption energy and accelerates electron transport, thus promoting catalytic reactions. The synergistic effect generated by interface engineering and P doping endows P-NiSe/MoSe<sub>2</sub>@NF with excellent HER performance, which is consistent with the results of the TEM, DFT, and XPS studies.

## Conclusions

In summary, we report P-doped NiSe/2H-MoSe<sub>2</sub> nanorod arrays obtained by the strategy of interface engineering and P doping with a special structure of nanoparticles on nanorods, which effectively accelerates hydrogen production under alkaline conditions. Benefiting from the exposure of more active sites, rapid charge transfer, and the interfacial effects arising from the interfaces between NiSe and 2H-MoSe<sub>2</sub> in the heterostructure, as well as the optimized electronic structure and hydrogen adsorption energy achieved by P doping, the prepared P-NiSe/MoSe<sub>2</sub>@NF possesses better HER performance than many recently reported TMSe catalysts under alkaline conditions. Specifically, P-NiSe/MoSe<sub>2</sub>@NF requires  $\eta_{10}$  and  $\eta_{100}$  values of 43 mV and 182 mV, respectively, for the HER and exhibits durability for over 30 h. This work provides a hopeful approach for the rational preparation of catalysts with multi-interface heterostructures and better electronic structures.

## Experimental

### Chemicals

All chemicals were not purified further and were used in their raw state. Nickel(II) nitrate hexahydrate [Ni(NO<sub>3</sub>)<sub>2</sub>·6H<sub>2</sub>O, Guangzhou Chemical Reagent Factory Co. Ltd]; sodium molybdate dihydrate (Na<sub>2</sub>MoO<sub>4</sub>·2H<sub>2</sub>O, Shanghai Aladdin Biochemical Technology Co. Ltd); selenium powder (Se, Shanghai Aladdin Biochemical Technology Co. Ltd); sodium hypophosphite (NaH<sub>2</sub>PO<sub>2</sub>, Macklin Ltd); hydrochloric acid (HCl, 36.0%, Guangzhou Chemical Reagent Factory Co. Ltd); potassium hydroxide (KOH, Shanghai Aladdin Biochemical Technology Co. Ltd); and Ni foam (NF, areal density 320 g cm<sup>-2</sup>, pore density 110 PPI, Suzhou Taili Material Technology Co. Ltd) were used as received. Ultrapure water with resistivity >18 MΩ cm<sup>-1</sup> was used throughout the experiments.

### Synthesis of the NiMoO<sub>4</sub>@NF and Ni(OH)<sub>2</sub>@NF precursors

To remove the surface oxides, bare NF (2 cm × 3 cm) was first ultrasonicated in hydrochloric acid (6 M) and then cleaned multiple times with ethanol and DI water. In a 50 mL Teflon autoclave, the purged NF was immersed in a 20 mL solution containing 290.8 mg Ni(NO<sub>3</sub>)<sub>2</sub>·6H<sub>2</sub>O and 121 mg Na<sub>2</sub>MoO<sub>4</sub>·2H<sub>2</sub>O, and then hydrothermally treated at 150 °C for 2 h. The Ni(OH)<sub>2</sub>@NF precursors were synthesized by the same procedure without Na<sub>2</sub>MoO<sub>4</sub>·2H<sub>2</sub>O.

### Synthesis of P-NiSe/MoSe<sub>2</sub>@NF and the other contrast catalysts

Mixed powder containing 200 mg selenium powder and 20 mg NaH<sub>2</sub>PO<sub>2</sub> and the NiMoO<sub>4</sub>@NF precursor were positioned upstream and downstream of the porcelain boat, respectively. After that, the porcelain boat was positioned at the center of a tube furnace, heated to 350 °C at a heating rate of 5 °C min<sup>-1</sup> and then held for 2 hours. A 5% H<sub>2</sub>-Ar reduction gas was used throughout the process, and P-NiSe/MoSe<sub>2</sub>@NF was obtained after naturally cooling to room temperature in the tube furnace. To investigate the optimal amount of phosphorus doping, 10 mg, 20 mg, and 30 mg NaH<sub>2</sub>PO<sub>2</sub> were used, and the prepared samples were named P-NiSe/MoSe<sub>2</sub>@NF-1, P-NiSe/MoSe<sub>2</sub>@NF-2, and P-NiSe/MoSe<sub>2</sub>@NF-3, respectively. For comparison, NiSe/MoSe<sub>2</sub>@NF was synthesized in a similar way as P-NiSe/MoSe<sub>2</sub>@NF but without the use of NaH<sub>2</sub>PO<sub>2</sub> during the annealing process. Ni<sub>x</sub>Se<sub>y</sub>/NF was synthesized in the same way as NiSe/MoSe<sub>2</sub>@NF, using the precursor but without adding molybdenum sources.

### Electrochemical measurements

Electrocatalytic performance tests were performed on an electrochemical workstation (Ivium V89105 and CHI 660E) using a three-electrode system in a 1.0 M KOH solution. The working electrode, counter electrode, and reference electrode were the prepared catalyst material, carbon rod, and mercuric oxide electrode, respectively. All potentials were further corrected with 80% *iR* correction and converted using the following equation:

$$E_{\text{RHE}} = 0.098 + 0.059 \times \text{pH} + E_{\text{Hg}/\text{HgO}}$$

The double layer capacitance ( $C_{\text{dl}}$ ) was acquired by processing the cyclic voltammetry (CV) curves at various scan rates (20, 40, 60, 80, 100 mV s<sup>-1</sup>) over a potential range of 0.18–0.28 V (*vs.* RHE). Electrochemical impedance spectroscopy (EIS) was performed at an overpotential of 600 mV in a frequency range of 10<sup>5</sup>–10<sup>-2</sup> Hz. The long-term durability was tested by chronopotentiometry (CP) measurements.

### Characterization

The phase composition was studied with a Japan X-ray diffractometer (XRD, Rigaku, D/Max-III) equipped with Cu K $\alpha$  radiation ( $\lambda = 1.5418 \text{ \AA}$ ). Scanning electron microscopy (SEM) was carried out on a HITACHI SU8010 field emission scanning electron microscope (FESEM). The Raman spectra were exam-

ined on a Renishaw inVia Qontor with a 532 nm laser as the excitation light source. X-ray photoelectron spectroscopy (XPS) was conducted using a SHIMADZU AXIS SUPRA with a monochromatic Al K $\alpha$  source. Transmission electron microscopy (TEM) was performed on an FEL Tecnai F30 apparatus. Elemental mapping was performed with an energy-dispersive X-ray spectrometer (EDX) attached to the FEL Tecnai F30 instrument.

### Theoretical calculations

All the density functional theory (DFT) calculations were performed with the Vienna *ab initio* simulation package (VASP).<sup>52,53</sup> The electron exchange–correlation was described by the generalized gradient approximation (GGA)<sup>54</sup> of the Perdew–Burke–Ernzerhof (PBE) functional.<sup>55</sup> Hubbard-*U* corrections were employed to calculate the on-site Coulomb repulsion for the Ni 3d electrons with  $U = 3.0$  eV.<sup>56</sup> The cut-off energy for the plane wave basis was fixed at 450 eV. A vacuum larger than 15 Å was applied to remove the adjacent image interactions. Grimme's DFT-D3 method was applied to modify the van der Waals (vdW) interaction between NiSe and MoSe<sub>2</sub>. Brillouin zone integration was conducted using a  $4 \times 4 \times 1$  *k*-point mesh for free-energy calculations. During the calculations of all the surfaces and slabs, all the structures were totally relaxed, with an energy tolerance of 0.03 eV Å<sup>-1</sup> on each atom. Dipole correction was employed.<sup>57,58</sup> The convergence tolerances for energy and force were 0.0005 eV and 0.03 eV Å<sup>-1</sup>, respectively.

### Conflicts of interest

There are no conflicts to declare.

### Acknowledgements

This work was supported by the Guangdong University of Technology Hundred Talents Program (No. 220418136) and Macao Young Scholars Program (AM2021009).

### References

- H. Sun, Z. Yan, F. Liu, W. Xu, F. Cheng and J. Chen, Self-Supported Transition-Metal-Based Electrocatalysts for Hydrogen and Oxygen Evolution, *Adv. Mater.*, 2020, **32**, 1806326.
- D. Du, S. Zhao, Z. Zhu, F. Li and J. Chen, Photo-excited Oxygen Reduction and Oxygen Evolution Reactions Enable a High-Performance Zn–Air Battery, *Angew. Chem., Int. Ed.*, 2020, **59**, 18140–18144.
- K. Tang, C. Yuan, Y. Xiong, H. Hu and M. Wu, Inverse-opal-structured hybrids of N, S-codoped-carbon-confined Co<sub>9</sub>S<sub>8</sub> nanoparticles as bifunctional oxygen electrocatalyst for on-chip all-solid-state rechargeable Zn-air batteries, *Appl. Catal., B*, 2020, **260**, 118209.
- J. Tang, D. Chen, Q. Yao, J. Xie and J. Yang, Recent advances in noble metal-based nanocomposites for electrochemical reactions, *Mater. Today Energy*, 2017, **6**, 115–127.
- W. Luo, Y. Wang and C. Cheng, Ru-based electrocatalysts for hydrogen evolution reaction: Recent research advances and perspectives, *Mater. Today Phys.*, 2020, **15**, 100274.
- R. Wang, Y. Yang, Z. Sun and X. Lu, Ga doped Ni<sub>3</sub>S<sub>2</sub> ultrathin nanosheet arrays supported on Ti<sub>3</sub>C<sub>2</sub>-MXene/Ni foam: An efficient and stable 3D electrocatalyst for oxygen evolution reaction, *Int. J. Hydrogen Energy*, 2022, **47**, 2958–2966.
- K. Tang, H. Hu, Y. Xiong, L. Chen, J. Zhang, C. Yuan and M. Wu, Hydrophobization Engineering of the Air–Cathode Catalyst for Improved Oxygen Diffusion towards Efficient Zinc–Air Batteries, *Angew. Chem.*, 2022, **61**, e202202671.
- S. Zhang, G. Gao, H. Zhu, L. Cai, X. Jiang, S. Lu, F. Duan, W. Dong, Y. Chai and M. Du, In situ interfacial engineering of nickel tungsten carbide Janus structures for highly efficient overall water splitting, *Sci. Bull.*, 2020, **65**, 640–650.
- S. Dutta, A. Indra, Y. Feng, H. Han and T. Song, Promoting electrocatalytic overall water splitting with nanohybrid of transition metal nitride-oxynitride, *Appl. Catal., B*, 2019, **241**, 521–527.
- J. Hei, G. Xu, B. Wei, L. Zhang, H. Ding and D. Liu, NiFeP nanosheets on N-doped carbon sponge as a hierarchically structured bifunctional electrocatalyst for efficient overall water splitting, *Appl. Surf. Sci.*, 2021, **549**, 149297.
- H. Liu, D. Zhao, M. Dai, X. Zhu, F. Qu, A. Umar and X. Wu, PEDOT decorated CoNi<sub>2</sub>S<sub>4</sub> nanosheets electrode as bifunctional electrocatalyst for enhanced electrocatalysis, *Chem. Eng. J.*, 2022, **428**, 131183.
- Z. Liu, C. Zhang, H. Liu and L. Feng, Efficient synergism of NiSe<sub>2</sub> nanoparticle/NiO nanosheet for energy-relevant water and urea electrocatalysis, *Appl. Catal., B*, 2020, **276**, 119165.
- Y.-N. Zhou, Y.-R. Zhu, X.-T. Yan, Y.-N. Cao, J. Li, B. Dong, M. Yang, Q.-Z. Li, C.-G. Liu and Y.-M. Chai, Hierarchical CoSeS nanostructures assisted by Nb doping for enhanced hydrogen evolution reaction, *Chin. J. Catal.*, 2021, **42**, 431–438.
- Y. Yan, P. Wang, J. Lin, J. Cao and J. Qi, Modification strategies on transition metal-based electrocatalysts for efficient water splitting, *J. Energy Chem.*, 2021, **58**, 446–462.
- Z. Zhu, Y. Ni, Q. Lv, J. Geng, W. Xie, F. Li and J. Chen, Surface plasmon mediates the visible light-responsive lithium–oxygen battery with Au nanoparticles on defective carbon nitride, *Proc. Natl. Acad. Sci. U. S. A.*, 2021, **118**, e2024619118.
- M. Zhu, Q. Yan, Y. Xue, Y. Yan, K. Zhu, K. Ye, J. Yan, D. Cao, H. Xie and G. Wang, Free-Standing P-Doped NiSe<sub>2</sub>/MoSe<sub>2</sub> Catalyst for Efficient Hydrogen Evolution in Acidic and Alkaline Media, *ACS Sustainable Chem. Eng.*, 2022, **10**, 279–287.
- Y. Rao, S. Wang, R. Zhang, S. Jiang, S. Chen, Y. Yu, S. Bao, M. Xu, Q. Yue, H. Xin and Y. Kang, Nanoporous V-Doped

- Ni<sub>5</sub>P<sub>4</sub> Microsphere: A Highly Efficient Electrocatalyst for Hydrogen Evolution Reaction at All pH, *ACS Appl. Mater. Interfaces*, 2020, **12**, 37092–37099.
- 18 W. Yang, S. Wang, K. Zhao, Y. Hua, J. Qiao, W. Luo, L. Li, J. Hao and W. Shi, Phosphorus doped nickel selenide for full device water splitting, *J. Colloid Interface Sci.*, 2021, **602**, 115–122.
- 19 X. Luo, P. Ji, P. Wang, R. Cheng, D. Chen, C. Lin, J. Zhang, J. He, Z. Shi, N. Li, S. Xiao and S. Mu, Interface Engineering of Hierarchical Branched Mo-Doped Ni<sub>3</sub>S<sub>2</sub>/Ni<sub>x</sub>P<sub>y</sub> Hollow Heterostructure Nanorods for Efficient Overall Water Splitting, *Adv. Energy Mater.*, 2020, **10**, 1903891.
- 20 W. Feng, M. Bu, S. Kan, X. Gao, A. Guo, H. Liu, L. Deng and W. Chen, Interfacial hetero-phase construction in nickel/molybdenum selenide hybrids to promote the water splitting performance, *Appl. Mater. Today*, 2021, **25**, 101175.
- 21 H. Zhang, B. Xi, Y. Gu, W. Chen and S. Xiong, Interface engineering and heterometal doping Mo-NiS/Ni(OH)<sub>2</sub> for overall water splitting, *Nano Res.*, 2021, **14**, 3466–3473.
- 22 Y. Li, M. B. Majewski, S. M. Islam, S. Hao, A. A. Murthy, J. G. DiStefano, E. D. Hanson, Y. Xu, C. Wolverton, M. G. Kanatzidis, M. R. Wasielewski, X. Chen and V. P. Dravid, Morphological Engineering of Winged Au@MoS<sub>2</sub> Heterostructures for Electrocatalytic Hydrogen Evolution, *Nano Lett.*, 2018, **18**, 7104–7110.
- 23 Y. Ma, M. Chen, H. Geng, H. Dong, P. Wu, X. Li, G. Guan and T. Wang, Synergistically Tuning Electronic Structure of Porous β-Mo<sub>2</sub>C Spheres by Co Doping and Mo-Vacancies Defect Engineering for Optimizing Hydrogen Evolution Reaction Activity, *Adv. Funct. Mater.*, 2020, **30**, 2000561.
- 24 J. Lin, H. Wang, J. Cao, F. He, J. Feng and J. Qi, Engineering Se vacancies to promote the intrinsic activities of P doped NiSe<sub>2</sub> nanosheets for overall water splitting, *J. Colloid Interface Sci.*, 2020, **571**, 260–266.
- 25 X. Xing, X. Wang, C. Wu, Y. Lu and M. Yan, Room temperature ferromagnetism and its origin for amorphous MoSe<sub>2</sub> nanoflowers, *Appl. Phys. Lett.*, 2018, **112**, 122407.
- 26 Z. Zhang, S. Ye, J. Ji, Z. Li and F. Wang, Core/shell -structured NiMoO<sub>4</sub>@MoSe<sub>2</sub>/Ni<sub>x</sub>Se<sub>y</sub> Nanorod on Ni Foam as a Bifunctional Electrocatalyst for Efficient Overall Water Splitting, *Colloids Surf., A*, 2020, **599**, 124888.
- 27 L. Liu, J. Xu, J. Sun, S. He, K. Wang, Y. Chen, S. Dou, Z. Du, H. Du, W. Ai and W. Huang, A stable and ultrafast K ion storage anode based on phase-engineered MoSe<sub>2</sub>, *ChemComm*, 2021, **57**, 3885–3888.
- 28 X. Du, G. Ma and X. Zhang, Experimental and Theoretical Understanding on Electrochemical Activation Processes of Nickel Selenide for Excellent Water-Splitting Performance: Comparing the Electrochemical Performances with M-NiSe (M = Co, Cu, and V), *ACS Sustainable Chem. Eng.*, 2019, **7**, 19257–19267.
- 29 T.-Y. Chen, B. Vedhanarayanan, S.-Y. Lin, L.-D. Shao, Z. Sofer, J.-Y. Lin and T.-W. Lin, Electrodeposited NiSe on a forest of carbon nanotubes as a free-standing electrode for hybrid supercapacitors and overall water splitting, *J. Colloid Interface Sci.*, 2020, **574**, 300–311.
- 30 Y. Li, D. Yan, Y. Zou, C. Xie, Y. Wang, Y. Zhang and S. Wang, Rapidly engineering the electronic properties and morphological structure of NiSe nanowires for the oxygen evolution reaction, *J. Mater. Chem. A*, 2017, **5**, 25494–25500.
- 31 B. Fei, Z. Chen, J. Liu, H. Xu, X. Yan, H. Qing, M. Chen and R. Wu, Ultrathinning Nickel Sulfide with Modulated Electron Density for Efficient Water Splitting, *Adv. Energy Mater.*, 2020, **10**, 2001963.
- 32 L. Gao, Z. Liu, J. Ma, L. Zhong, Z. Song, J. Xu, S. Gan, D. Han and L. Niu, NiSe@NiO<sub>x</sub> core-shell nanowires as a non-precious electrocatalyst for upgrading 5-hydroxymethylfurfural into 2,5-furandicarboxylic acid, *Appl. Catal., B*, 2020, **261**, 118235.
- 33 X. Yan, M. Gu, Y. Wang, L. Xu, Y. Tang and R. Wu, *In situ* growth of Ni nanoparticle-encapsulated N-doped carbon nanotubes on carbon nanorods for efficient hydrogen evolution electrocatalysis, *Nano Res.*, 2020, **13**, 975–982.
- 34 H. Zhao, W. Wang, Y. Du, Y. Yang, M. Wang, S. Li, R. Chen, Y. Liu and L. Wang, Se doped nickel-molybdenum bimetal sulfide with enhanced electrochemical activity for hydrogen evolution reaction, *Int. J. Hydrogen Energy*, 2021, **46**, 10763–10772.
- 35 J. Hu, Y. Q. Liang, S. L. Wu, Z. Y. Li, C. S. Shi, S. Y. Luo, H. J. Sun, S. L. Zhu and Z. D. Cui, Hierarchical nickel-iron layered double hydroxide composite electrocatalyst for efficient oxygen evolution reaction, *Mater. Today Nano*, 2022, **17**, 100150.
- 36 S. Deng, F. Yang, Q. Zhang, Y. Zhong, Y. Zeng, S. Lin, X. Wang, X. Lu, C.-Z. Wang, L. Gu, X. Xia and J. Tu, Phase Modulation of (1T-2H)-MoSe<sub>2</sub>/TiC-C Shell/Core Arrays via Nitrogen Doping for Highly Efficient Hydrogen Evolution Reaction, *Adv. Mater.*, 2018, **30**, 1802223.
- 37 Y. Wang, Y. Wang, W. Kang, D. Cao, C. Li, D. Cao, Z. Kang, D. Sun, R. Wang and Y. Cao, TiO<sub>2</sub>-Coated Interlayer-Expanded MoSe<sub>2</sub>/Phosphorus-Doped Carbon Nanospheres for Ultrafast and Ultralong Cycling Sodium Storage, *Adv. Sci.*, 2019, **6**, 1801222.
- 38 X. Wang, B. Zheng, B. Yu, B. Wang, W. Hou, W. Zhang and Y. Chen, *In situ* synthesis of hierarchical MoSe<sub>2</sub>-CoSe<sub>2</sub> nanotubes as an efficient electrocatalyst for the hydrogen evolution reaction in both acidic and alkaline media, *J. Mater. Chem. A*, 2018, **6**, 7842–7850.
- 39 W. Wang, L. Huai, S. Wu, J. Shan, J. Zhu, Z. Liu, L. Yue and Y. Li, Ultrahigh-Volumetric-Energy-Density Lithium-Sulfur Batteries with Lean Electrolyte Enabled by Cobalt-Doped MoSe<sub>2</sub>/Ti<sub>3</sub>C<sub>2</sub>T<sub>x</sub> MXene Bifunctional Catalyst, *ACS Nano*, 2021, **15**, 11619–11633.
- 40 S. Deng, C. Ai, M. Luo, B. Liu, Y. Zhang, Y. Li, S. Lin, G. Pan, Q. Xiong, Q. Liu, X. Wang, X. Xia and J. Tu, Coupled Biphasic (1T-2H)-MoSe<sub>2</sub> on Mold Spore Carbon for Advanced Hydrogen Evolution Reaction, *Small*, 2019, **15**, 1901796.
- 41 N. Li, J. Wu, Y. Lu, Z. Zhao, H. Zhang, X. Li, Y.-Z. Zheng and X. Tao, Stable multiphasic 1T/2H MoSe<sub>2</sub> nanosheets

- integrated with 1D sulfide semiconductor for drastically enhanced visible-light photocatalytic hydrogen evolution, *Appl. Catal., B*, 2018, **238**, 27–37.
- 42 J. Yu, Q. Li, Y. Li, C.-Y. Xu, L. Zhen, V. P. Dravid and J. Wu, Ternary Metal Phosphide with Triple-Layered Structure as a Low-Cost and Efficient Electrocatalyst for Bifunctional Water Splitting, *Adv. Funct. Mater.*, 2016, **26**, 7644–7651.
- 43 J.-J. Duan, R.-L. Zhang, J.-J. Feng, L. Zhang, Q.-L. Zhang and A.-J. Wang, Facile synthesis of nanoflower-like phosphorus-doped  $\text{Ni}_3\text{S}_2/\text{CoFe}_2\text{O}_4$  arrays on nickel foam as a superior electrocatalyst for efficient oxygen evolution reaction, *J. Colloid Interface Sci.*, 2021, **581**, 774–782.
- 44 F. Yu, H. Zhou, Y. Huang, J. Sun, F. Qin, J. Bao, W. A. Goddard, S. Chen and Z. Ren, High-performance bifunctional porous non-noble metal phosphide catalyst for overall water splitting, *Nat. Commun.*, 2018, **9**, 2551.
- 45 J. Yu, W.-J. Li, G. Kao, C.-Y. Xu, R. Chen, Q. Liu, J. Liu, H. Zhang and J. Wang, *In situ* growth of CNTs encapsulating P-doped  $\text{NiSe}_2$  nanoparticles on carbon framework as efficient bifunctional electrocatalyst for overall water splitting, *J. Energy Chem.*, 2021, **60**, 111–120.
- 46 Z. Zhu, J. Hao, H. Zhu, S. Sun, F. Duan, S. Lu and M. Du, In Situ Fabrication of Electrospun Carbon Nanofibers–Binary Metal Sulfides as Freestanding Electrode for Electrocatalytic Water Splitting, *Adv. Fiber Mater.*, 2021, **3**, 117–127.
- 47 J. Wei, M. Zhou, A. Long, Y. Xue, H. Liao, C. Wei and Z. J. Xu, Heterostructured Electrocatalysts for Hydrogen Evolution Reaction Under Alkaline Conditions, *Nanomicro Lett.*, 2018, **10**, 75.
- 48 Y. Guo, T. Park, J. W. Yi, J. Henzie, J. Kim, Z. Wang, B. Jiang, Y. Bando, Y. Sugahara, J. Tang and Y. Yamauchi, Nanoarchitectonics for Transition-Metal-Sulfide-Based Electrocatalysts for Water Splitting, *Adv. Mater.*, 2019, **31**, 1807134.
- 49 J. Hao, Z. Zhuang, K. Cao, G. Gao, C. Wang, F. Lai, S. Lu, P. Ma, W. Dong, T. Liu, M. Du and H. Zhu, Unraveling the electronegativity-dominated intermediate adsorption on high-entropy alloy electrocatalysts, *Nat. Commun.*, 2022, **13**, 2662.
- 50 S. Deng, Y. Zhong, Y. Zeng, Y. Wang, Z. Yao, F. Yang, S. Lin, X. Wang, X. Lu, X. Xia and J. Tu, Directional Construction of Vertical Nitrogen-Doped 1T-2H  $\text{MoSe}_2$ /Graphene Shell/Core Nanoflake Arrays for Efficient Hydrogen Evolution Reaction, *Adv. Mater.*, 2017, **29**, 1700748.
- 51 X. Guo, X. Wan, Q. Liu, Y. Li, W. Li and J. Shui, Phosphated IrMo bimetallic cluster for efficient hydrogen evolution reaction, *eScience*, 2022, **2**, 304–310.
- 52 G. Kresse and J. Furthmüller, Efficient iterative schemes for ab initio total-energy calculations using a plane-wave basis set, *Phys. Rev. B: Condens. Matter Mater. Phys.*, 1996, **54**, 11169–11186.
- 53 G. Kresse and J. Furthmüller, Efficiency of *ab initio* total energy calculations for metals and semiconductors using a plane-wave basis set, *Comput. Mater. Sci.*, 1996, **6**, 15–50.
- 54 P. E. Blöchl, Projector augmented-wave method, *Phys. Rev. B: Condens. Matter Mater. Phys.*, 1994, **50**, 17953–17979.
- 55 J. P. Perdew, K. Burke and M. Ernzerhof, Generalized Gradient Approximation Made Simple, *Phys. Rev. Lett.*, 1996, **77**, 3865–3868.
- 56 V. I. Anisimov, F. Aryasetiawan and A. I. Lichtenstein, First-principles calculations of the electronic structure and spectra of strongly correlated systems: the LDA+*U* method, *J. Phys.: Condens. Matter*, 1997, **9**, 767–808.
- 57 G. Makov and M. C. Payne, Periodic boundary conditions in ab initio calculations, *Phys. Rev. B: Condens. Matter Mater. Phys.*, 1995, **51**, 4014–4022.
- 58 J. Neugebauer and M. Scheffler, Adsorbate-substrate and adsorbate-adsorbate interactions of Na and K adlayers on Al(111), *Phys. Rev. B: Condens. Matter Mater. Phys.*, 1992, **46**, 16067–16080.